Supporting information for

Mechanistic Insights of Cycling Stability of Ferrocene Catholytes in Aqueous Redox Flow Batteries

Jian Luo,[a] Maowei Hu,[a] Wenda Wu,[a] Bing Yuan,[a,b] T. Leo Liu [a,*]
[a] The Department of Chemistry and Biochemistry, Utah State University, Logan, UT
[b] State Key Laboratory Base of Eco-chemical Engineering, College of Chemistry and Molecular Engineering, Qingdao University of Science and Technology, Qingdao 266042, China
*Corresponding Author: Leo.Liu@usu.edu

Contents

1. Full-cell RFB Studies

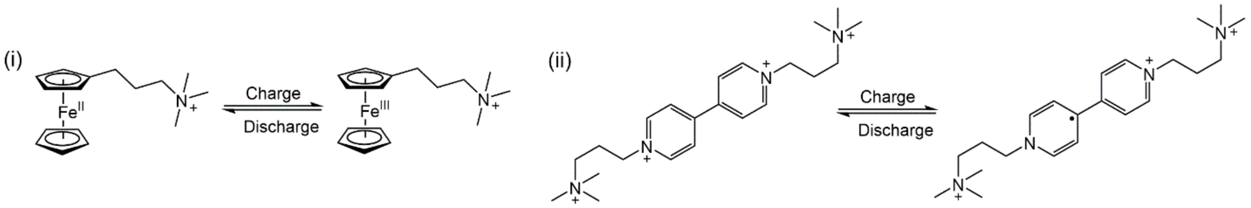

Scheme S1. Catholyte (i) and anolyte (ii) half-cell reactions of the ***C*$_3$-FcNCl**/$(NPr)_2VCl_4$ AORFB.

The half-cell RFB studies revealed the excellent stability of the ***C*$_3$-FcNCl** catholyte in AORFB applications. Full-cell AORFB demonstration of the ***C*$_3$-FcNCl** catholyte was performed by pairing with 1,1'-di(trimethylammonium-propyl) 4,4'-bipyridium tetrachloride, $(NPr)_2VCl_4$ ($E_{1/2}$ = -0.38 V versus NHE, Scheme S1), which has been reported as a robust anolyte in viologen/ferrocene and viologen/TEMPO AORFBs.[1-3] The ***C*$_3$-FcNCl**/$(NPr)_2VCl_4$ combination enabled a 0.75 V battery. In the full-cell AORFB configuration, 0.50 M ***C*$_3$-FcNCl** and 0.50 M $(NPr)_2VCl_4$ in a 1.00 M NH_4Cl supporting electrolyte were used as a catholyte and an anolyte, respectively. A piece of Selemion AMV anion-exchange membrane was used as a separator. The ***C*$_3$-FcNCl**/$(NPr)_2VCl_4$ AORFB was cycled with cut-off voltages at 1.05 V and 0.10 V for charge and discharge processes, respectively. The current rate performance was investigated at current densities from 10 to 50 $mA{\cdot}cm^{-2}$. As shown in Figure S15A, stable capacity retention was obtained in 5 continuous charge/discharge cycles under each current density. Meanwhile, the ***C*$_3$-FcNCl**/$(NPr)_2VCl_4$ AORFB showed excellent current rate performance, specifically, a small capacity decrease was observed with the current density increase from 10 $mA{\cdot}cm^{-2}$ (13.1 $Ah{\cdot}L^{-1}$, 98% capacity utilization) to 50 $mA{\cdot}cm^{-2}$ (12.4 $Ah{\cdot}L^{-1}$, 93% capacity utilization) (Figure S15A and S15B), which is benefitted from the high conductivity and fast electrochemical kinetics of the electrolytes. Figure S15C showed the battery efficiency data. Coulombic efficiency stayed nearly 100% at each current density. Upon increasing current density, the voltage efficiency and energy efficiency linearly decreased from 91% at 10 $mA{\cdot}cm^{-2}$ to 64% at 50 $mA{\cdot}cm^{-2}$. To measure the cycling stability of the ***C*$_3$-FcNCl**/$(NPr)_2VCl_4$ AORFB, a long cycling test was performed at 40 $mA{\cdot}cm^{-2}$ for 500 cycles (ca. 340 hours). During the long-term cycling test, the battery maintained nearly 100% coulombic efficiency, capacity utilization of 95%, and an energy efficiency of 70%. As shown in Figure S15D, the ***C*$_3$-FcNCl**/$(NPr)_2VCl_4$ AORFB delivered very stable cycling stability. Only 1.03% capacity fading was observed in 500 charge/discharge cycles, which is equivalent to 99.9979% per cycle or 99.927% per day capacity retention.

For comparison, ***C*$_1$-FcNCl** and ***C*$_2$-FcNCl** catholytes were also paired with the $(NPr)_2VCl_4$ anolyte for full-cell battery tests under the same conditions (Figure S13 and S14). Due to the higher redox potential of ***C*$_1$-FcNCl** (0.61 V, vs NHE) and ***C*$_2$-FcNCl** (0.44 V) than that of ***C*$_3$-FcNCl** (0.37 V), higher battery voltages were obtained for the ***C*$_1$-FcNCl**/$(NPr)_2VCl_4$ (0.99 V) and ***C*$_2$-FcNCl**/$(NPr)_2VCl_4$ (0.82 V) AORFB. The current rate performance of ***C*$_1$-FcNCl**/$(NPr)_2VCl_4$ and ***C*$_2$-FcNCl**/$(NPr)_2VCl_4$ AORFBs was not as good as that of ***C*$_3$-FcNCl**/$(NPr)_2VCl_4$ AORFB. Specifically, when the current density increased from 10 $mA{\cdot}cm^{-2}$ to 50 $mA{\cdot}cm^{-2}$, more significant capacity utilization decrease was observed for ***C*$_1$-FcNCl**/$(NPr)_2VCl_4$ (from 97% to 85%) and ***C*$_2$-FcNCl**/$(NPr)_2VCl_4$ (from 98% to 90%) AORFB than that of ***C*$_3$-FcNCl**/$(NPr)_2VCl_4$ AORFB (from

98% to 93%). Meanwhile, the energy efficiency decrease of **C_1-FcNCl**/$(NPr)_2VCl_4$ (from 91% at 10 $mA\cdot cm^{-2}$ to 59% at 50 $mA\cdot cm^{-2}$) and **C_2-FcNCl**/$(NPr)_2VCl_4$ (from 90% at 10 $mA\cdot cm^{-2}$ to 54% at 50 $mA\cdot cm^{-2}$) AORFBs was also more seriously than that of **C_3-FcNCl**/$(NPr)_2VCl_4$ AORFB (from 91% at 10 $mA\cdot cm^{-2}$ to 64% at 50 $mA\cdot cm^{-2}$). Similar as the half-cell test result, **C_1-FcNCl**/$(NPr)_2VCl_4$ AORFB displayed slight capacity fading in 5 continuous cycles at low current densities (10 and 20 $mA\cdot cm^{-2}$) (Figure S13). For the long-term cycling tests of the full-cell AORFBs, **C_1-FcNCl**/$(NPr)_2VCl_4$ AORFB showed much poorer stability than **C_2-FcNCl**/$(NPr)_2VCl_4$ and **C_3-FcNCl**/$(NPr)_2VCl_4$ AORFBs. In 500 charge/discharge cycles at 40 $mA\cdot cm^{-2}$, 13.53% capacity fading was observed for the **C_1-FcNCl**/$(NPr)_2VCl_4$ AORFB, however, only 2.57% and 1.03% capacity fading was observed for the **C_2-FcNCl**/$(NPr)_2VCl_4$ and **C_3-FcNCl**/$(NPr)_2VCl_4$ AORFBs, respectively. The capacity retention was equivalent to 99.9729% per cycle or 98.969% per day for **C_1-FcNCl**/$(NPr)_2VCl_4$ AORFB, 99.9949% per cycle or 99.816% per day for **C_2-FcNCl**/$(NPr)_2VCl_4$ AORFB and 99.9979% per cycle or 99.927% per day for **C_3-FcNCl**/$(NPr)_2VCl_4$ AORFB.

No active material degradation and cross-over were observed in post-cycling ^{1}H-NMR and CV analysis for the **C_2-FcNCl**/$(NPr)_2VCl_4$ and **C_3-FcNCl**/$(NPr)_2VCl_4$ AORFBs after 500 charge/discharge cycles (Figures S18 – S22), which further verified the improved stability of the **C_2-FcNCl**/$(NPr)_2VCl_4$ and **C_3-FcNCl**/$(NPr)_2VCl_4$ AORFBs. However, a new peak at $\delta = 2.55$ ppm was observed in the ^{1}H-NMR spectrum of the cycled **C_1-FcNCl** catholyte (Figure S16), which indicates the chemical degradation of **C_1-FcNCl** during charge/discharge cycling. The degradation of **C_1-FcNCl** catholyte was further confirmed by CV post-cycling analysis. As shown in Figure S22, there was an apparent current decrease for the cycled **C_1-FcNCl** catholyte, however, the CV curve of cycled $(NPr)_2VCl_4$ anolyte was almost overlapped with the original anolyte. It indicates that the capacity fading of **C_1-FcNCl**/$(NPr)_2VCl_4$ AORFB is mainly due to the decomposition of the **C_1-FcNCl** catholyte.

2. Supporting Data

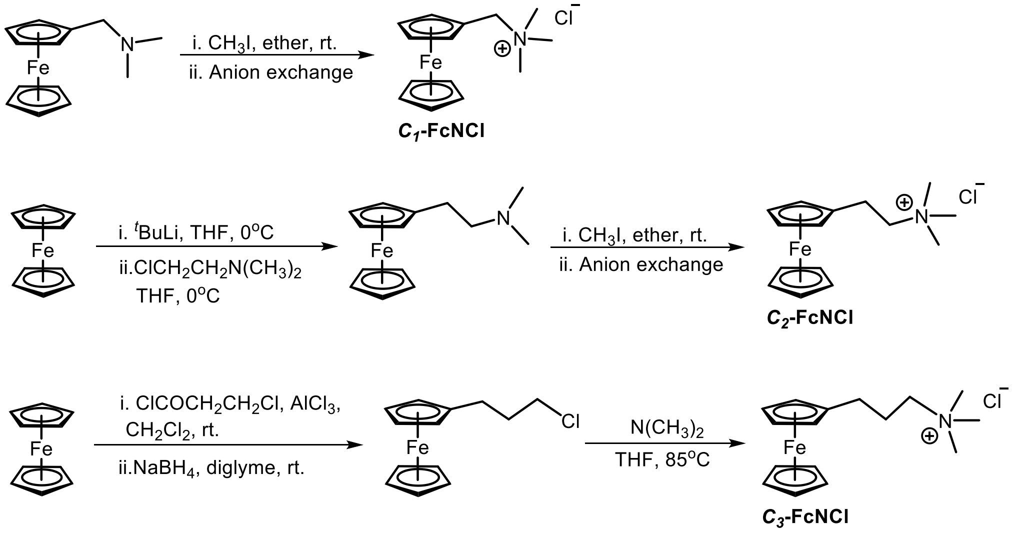

Scheme S1. Synthetic routes of the **C_x-FcNCl** compounds.

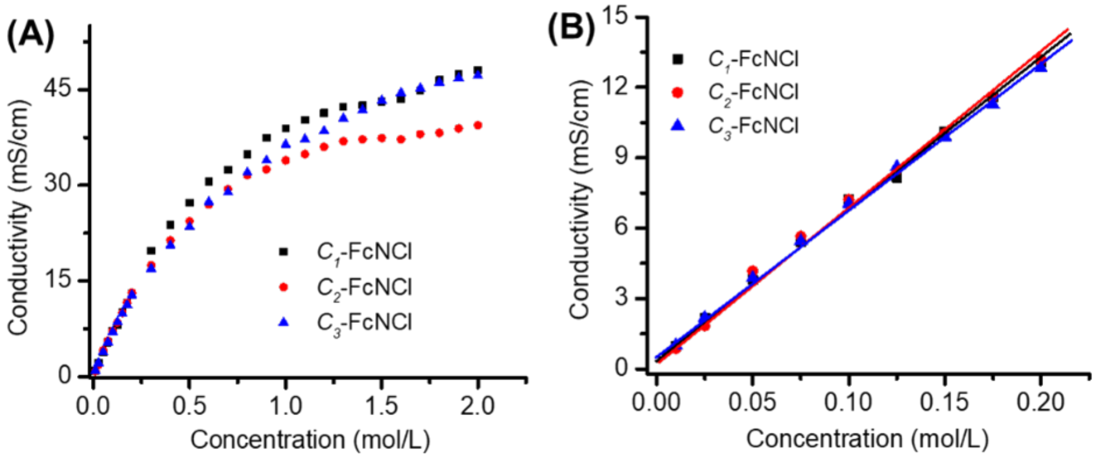

Figure S1. Conductivities of the **C_x-FcNCl** compounds in aqueous solutions. (A) Relationship between the concentration and ion conductivity of the **C_x-FcNCl** solutions. (B) Liner relationships between ion conductivity and concentration of **C_x-FcNCl** solutions from 10.0 mM to 200.0 mM.

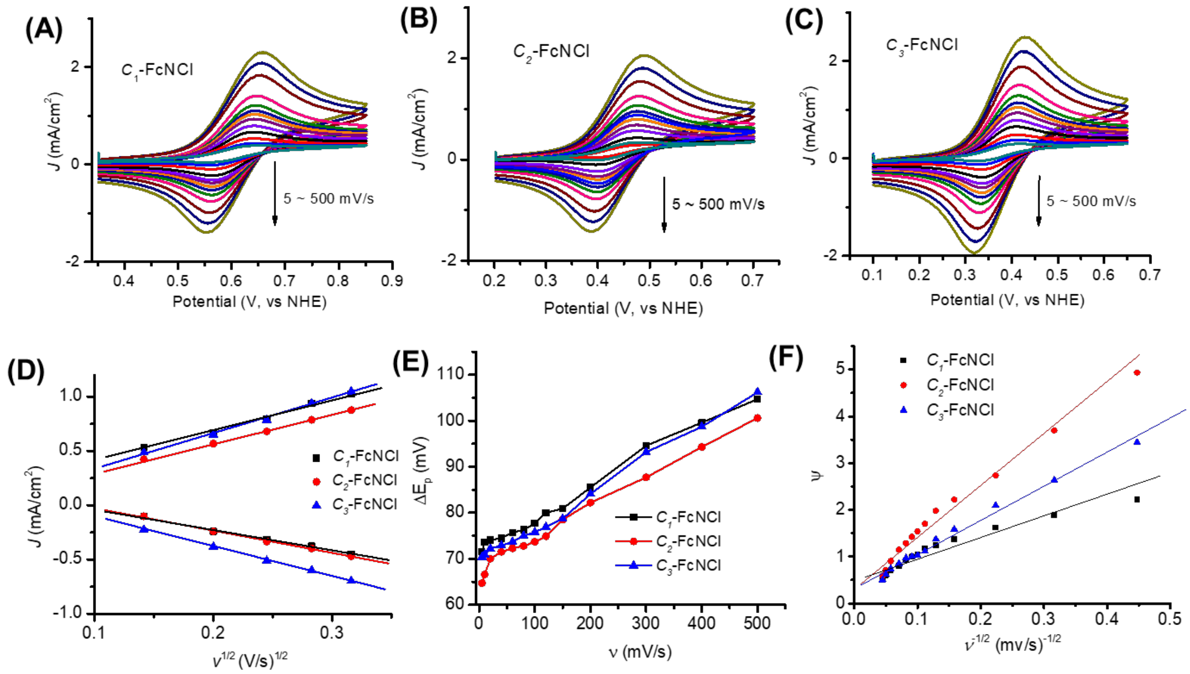

Figure S2. Nicholson's treatment for evaluation of the electron transfer rate constants k^0 from the cyclic voltammetry (CV) data of **C_x-FcNCl** compounds. CV curves of 4.0 mM **C_1-FcNCl** (A), **C_2-FcNCl** (B), and **C_3-FcNCl** (C) in 0.50 M NH_4Cl water solution at the scan rates of 5 − 500 mV·s^{-1} at room temperature; (D) Plot of *i vs.* $v^{1/2}$ with scan rate range 20 − 100 mV·s^{-1};(E) Plots of scan rate *v* vs. the peak-to-peak separation (ΔE_p); and (F) Plot of Ψ vs. $\upsilon^{-1/2}$.

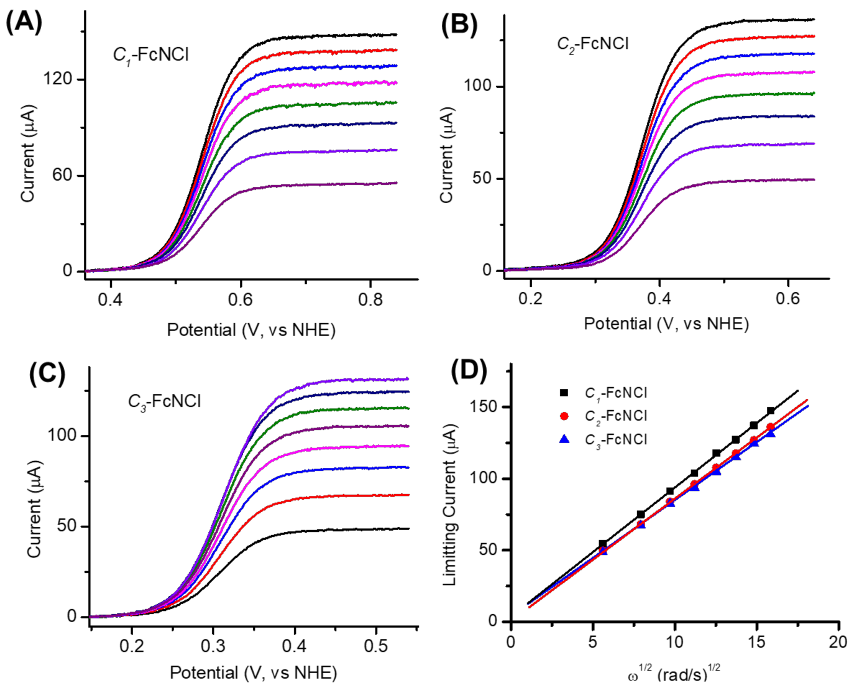

Figure S3. RDE studies of ***C_x*-FcNCl** compounds in a 0.50 M NH_4Cl supporting electrolyte. (A) 1.0 mM ***C_1*-FcNCl**; (B) ***C_2*-FcNCl**; (C) ***C_3*-FcNCl**; and (D) Plot of i *vs.* $\omega^{1/2}$.

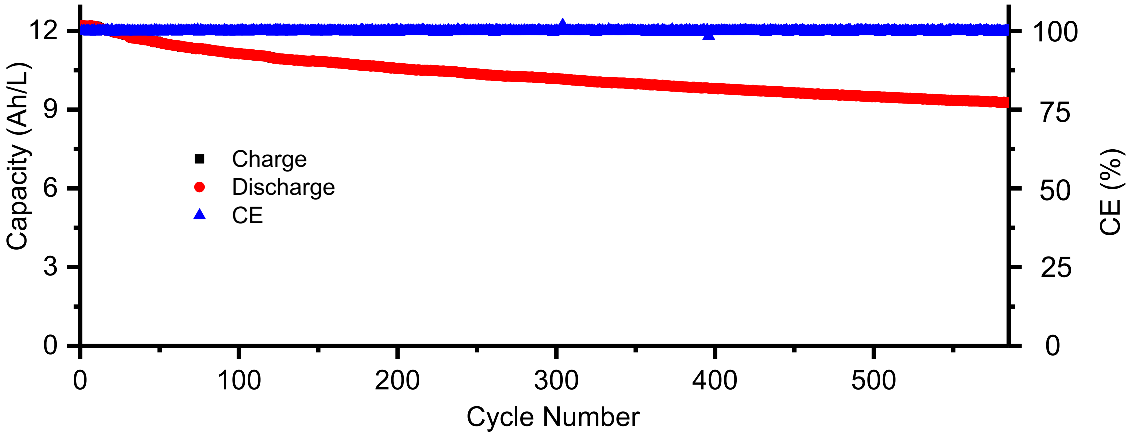

Figure S4. Charge/discharge capacity and CE of the ***C_1*-FcNCl** half-cell AORFB for 585 cycles (13 testing days) at 40 mA·cm^{-2}.

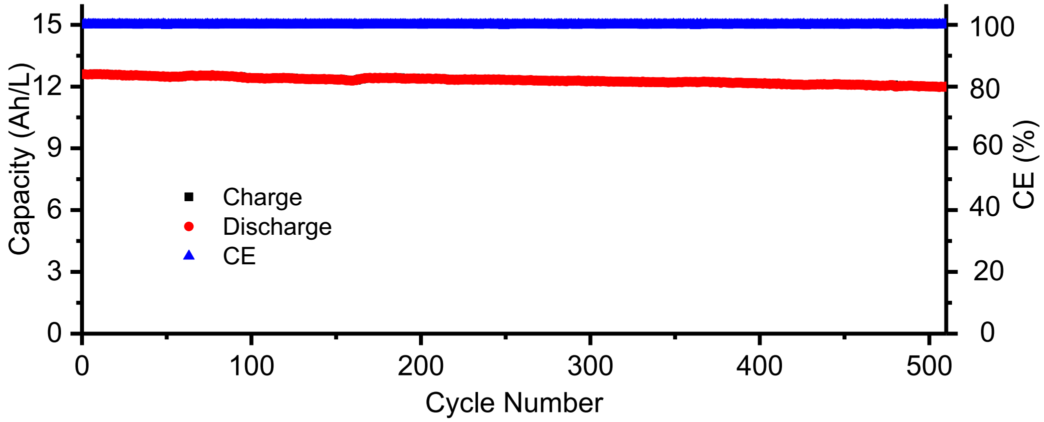

Figure S5. Charge/discharge capacity and CE of the ***C*$_2$-FcNCl** half-cell AORFB for 527 cycles (13 testing days) at 40 mA·cm^{-2}.

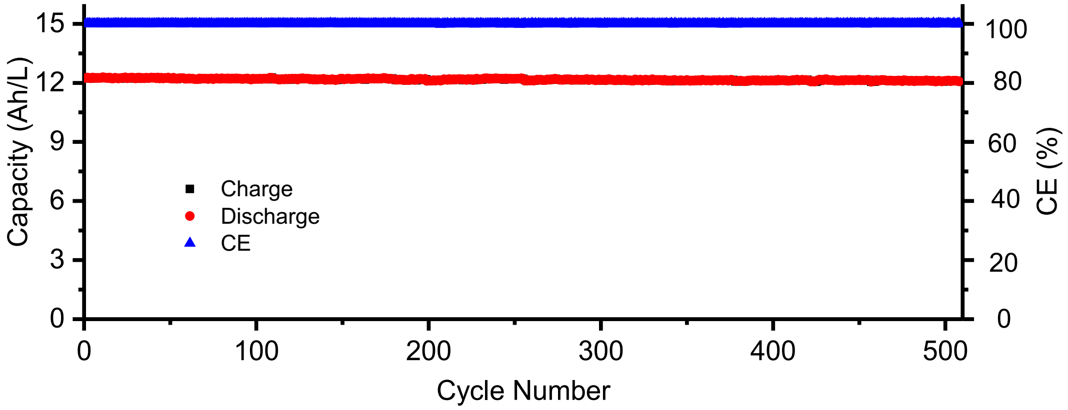

Figure S6. Charge/discharge capacity and CE of the ***C*$_3$-FcNCl** half-cell AORFB for 508 cycles (13 testing days) at 40 mA·cm^{-2}.

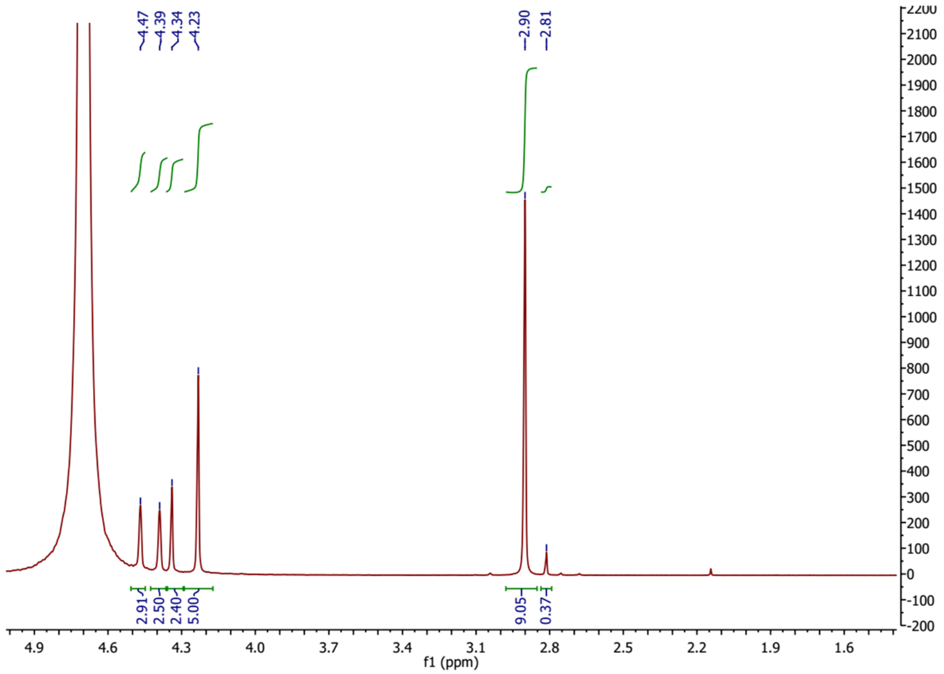

Figure S7. ^{1}H-NMR spectrum of ***C_1*-FcNCl** after the half-cell battery cycling.

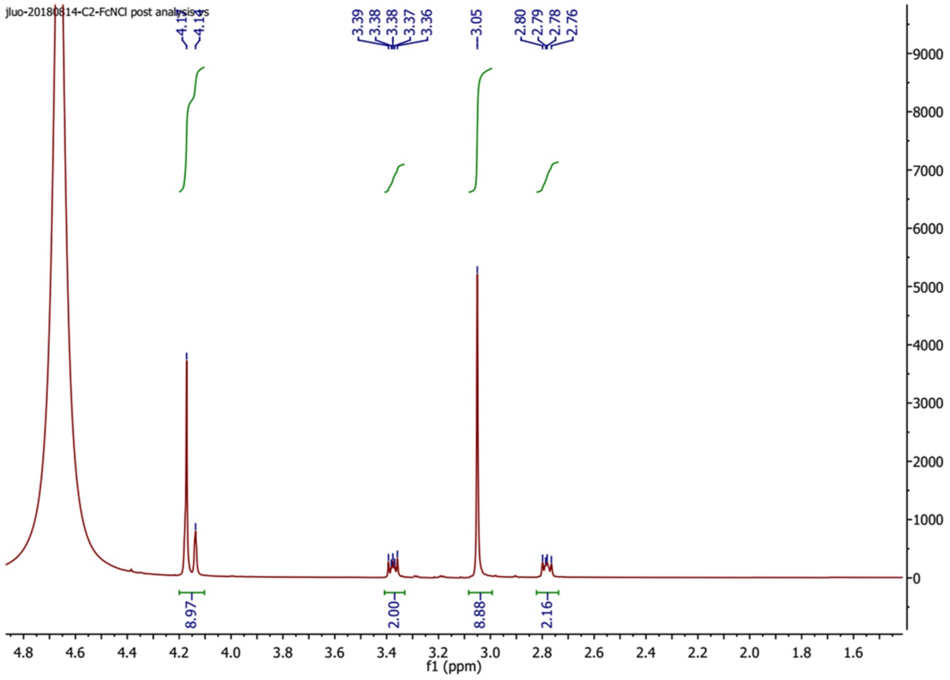

Figure S8. ^{1}H-NMR spectrum of ***C_2*-FcNCl** after the half-cell battery cycling.

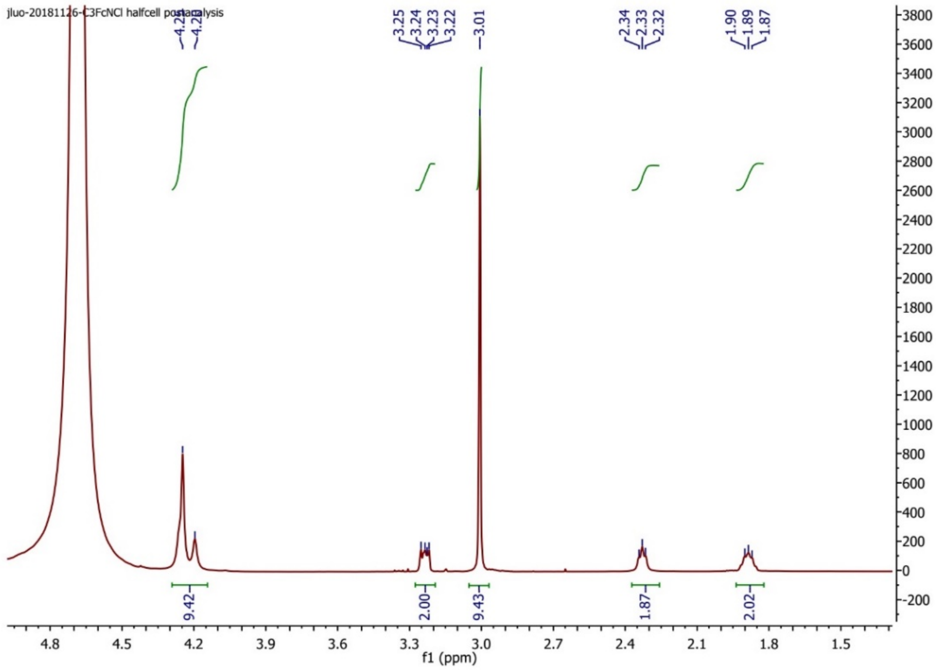

Figure S9. ^{1}H-NMR spectrum of ***C_3*-FcNCl** after the half-cell battery cycling.

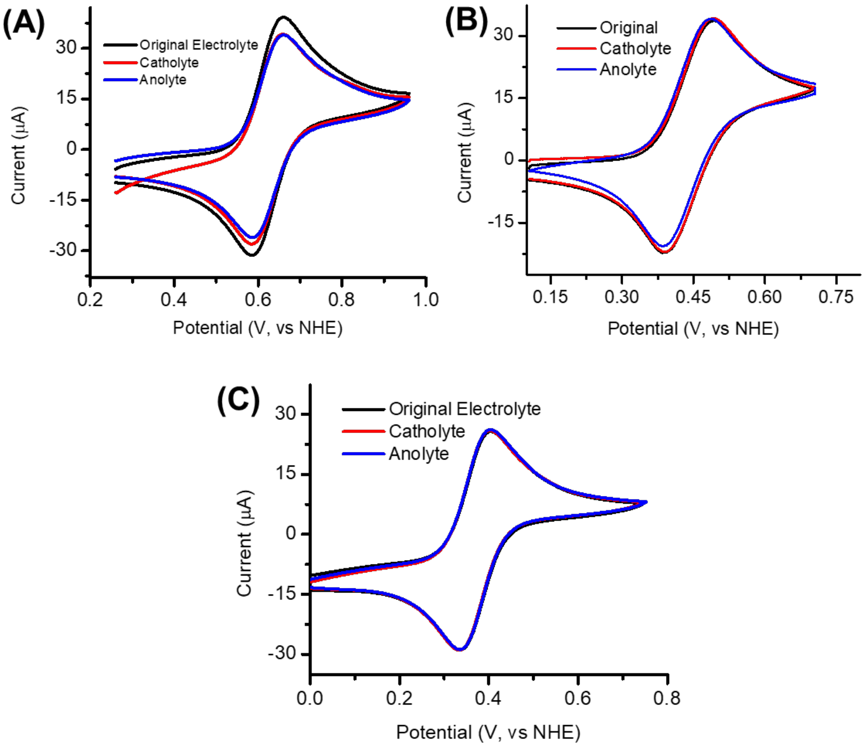

Figure S10. Post-cycling CV analysis of the ***C_x*-FcNCl** half-cell batteries. (A) ***C_1*-FcNCl**, (B) ***C_2*-FcNCl**, and (C) ***C_3*-FcNCl**.

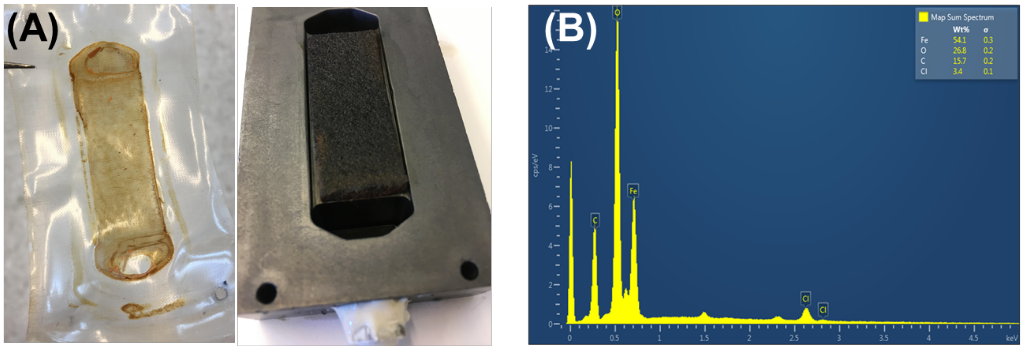

Figure S11. Post-analysis of cycled electrode and membrane for ***C₁*-FcNCl** half-cell RFB. (A) Pictures of separator and electrode; and (B) EDS spectrum of the cycled carbon felt.

Notes for Figure S11 (B): In the EDS, 2.02 : 1 (54.1 : 26.8) weight ratio between Fe and O elementals was found. It is between 1.16 : 1 of $Fe(OH)_3$ and 2.33 : 1 of Fe_2O_3, which is due to the partial dehydration of $Fe(OH)_3$ during the EDS sample preparation (80 °C 2 h under vacuum). 15.7 % of C is from the carbon felt background.

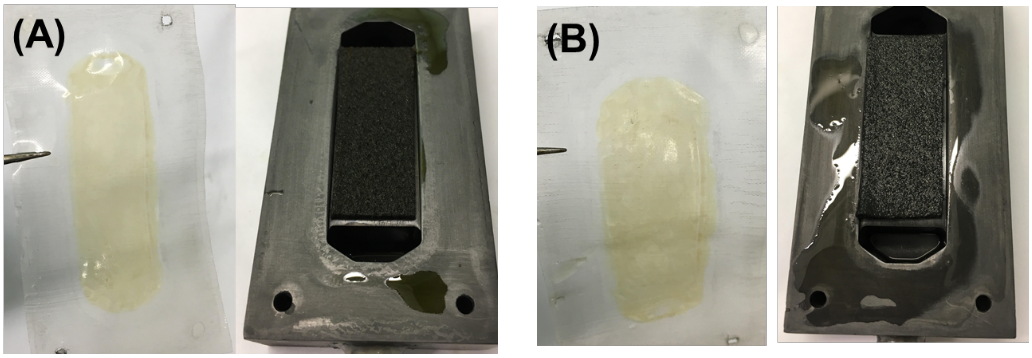

Figure S12. Post-cycling analysis of the cycled electrode and membrane for ***C₂*-FcNCl** and ***C₃*-FcNCl** half-cell RFB. Pictures of separator and electrode for cycled ***C₂*-FcNCl** (A) and ***C₃*-FcNCl** (B) half-cell RFBs.

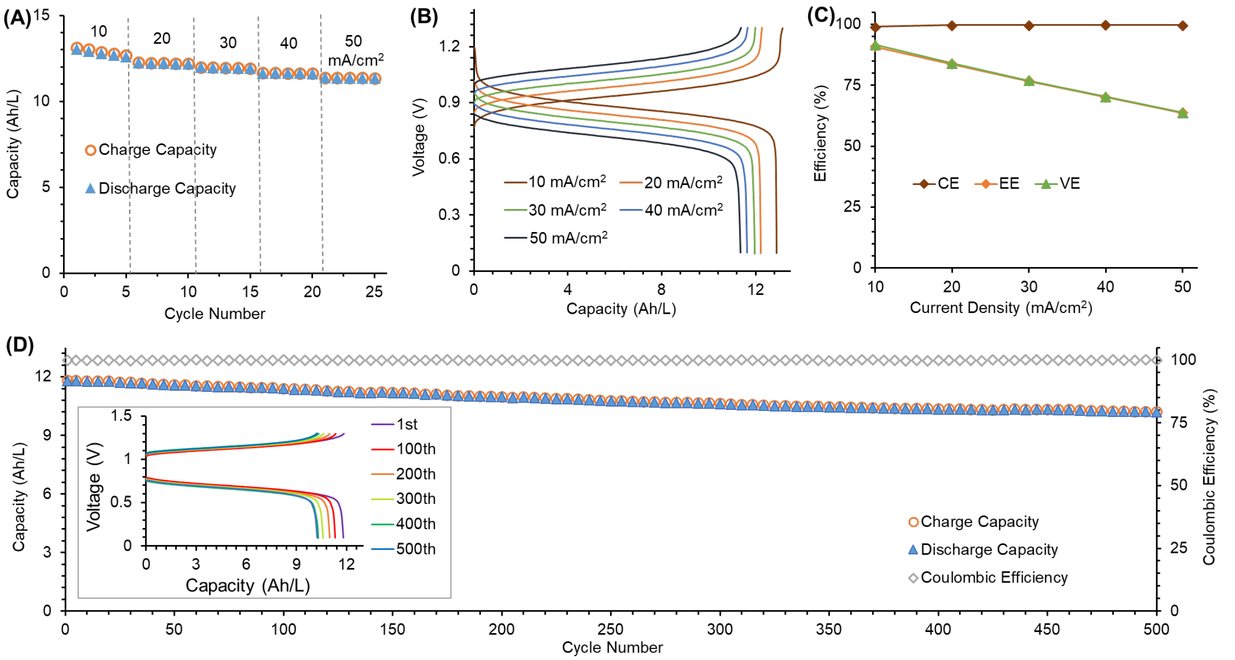

Figure S13. Full-cell RFB studies of the ***C_1*-FcNCl**/$(NPr)_2VCl_4$ AORFB. (A) Charge /discharge capacity versus cycling number from 10 to 50 mA·cm^{-2}. (B) Representative charge and discharge profiles under different current densities. (C) Coulombic efficiency (CE), energy efficiency (EE), and voltage efficiency (VE) under each current density. (D) Extended 500 cycles testing data at 40 mA·cm^{-2}. Condition: catholyte, 0.50 M ***C_1*-FcNCl** in 1.00 M NH_4Cl; anolyte, 0.50 M $(NPr)_2VCl_4$ in 1.00 M NH_4Cl; Selemion AMV anion-exchange membrane; pH was adjusted to 7.0 using diluted $NH_3•H_2O$ or HCl; 25 °C.

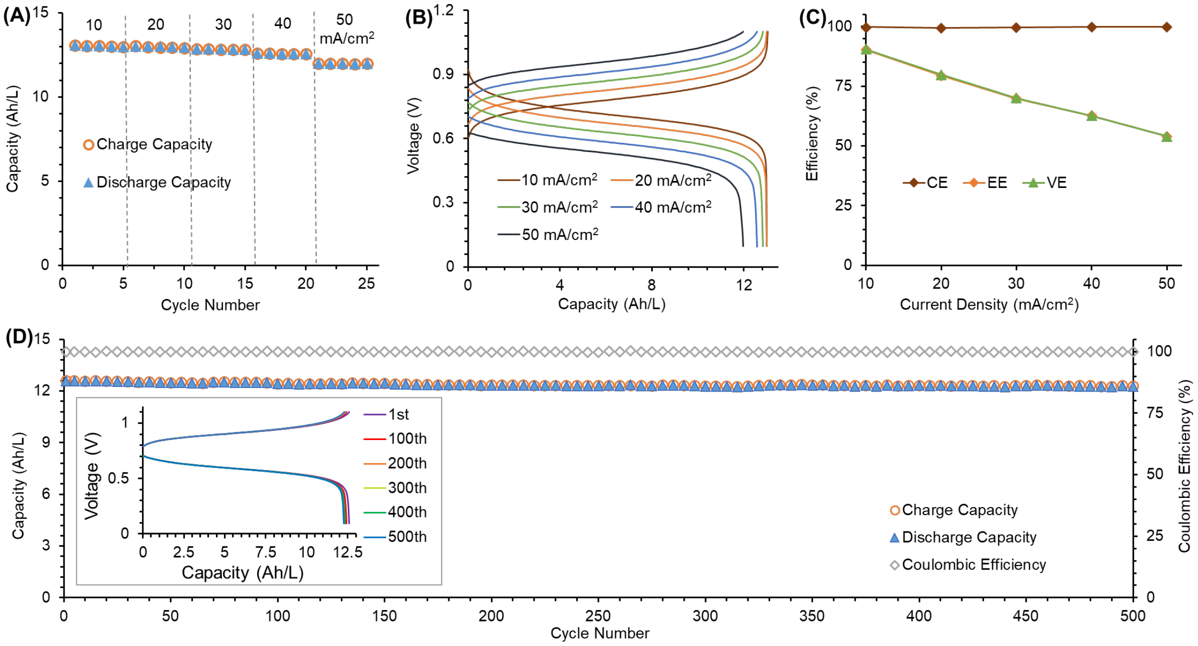

Figure S14. Full-cell RFB studies of the ***C₂*-FcNCl**/(NPr)$_2$VCl$_4$ AORFB. (A) Charge /discharge capacity versus cycling number from 10 to 50 mA·cm^{-2}. (B) Representative charge and discharge profiles under different current densities. (C) Coulombic efficiency (CE), energy efficiency (EE), and voltage efficiency (VE) under each current density. (D) Extended 500 cycles testing data at 40 mA·cm^{-2}. Condition: catholyte, 0.50 M ***C₂*-FcNCl** in 1.00 M NH_4Cl; anolyte, 0.50 M (NPr)$_2$VCl$_4$ in 1.00 M NH_4Cl; Selemion AMV anion-exchange membrane; pH was adjusted to 7.0 using diluted NH_3•H_2O or HCl; 25 ^{o}C.

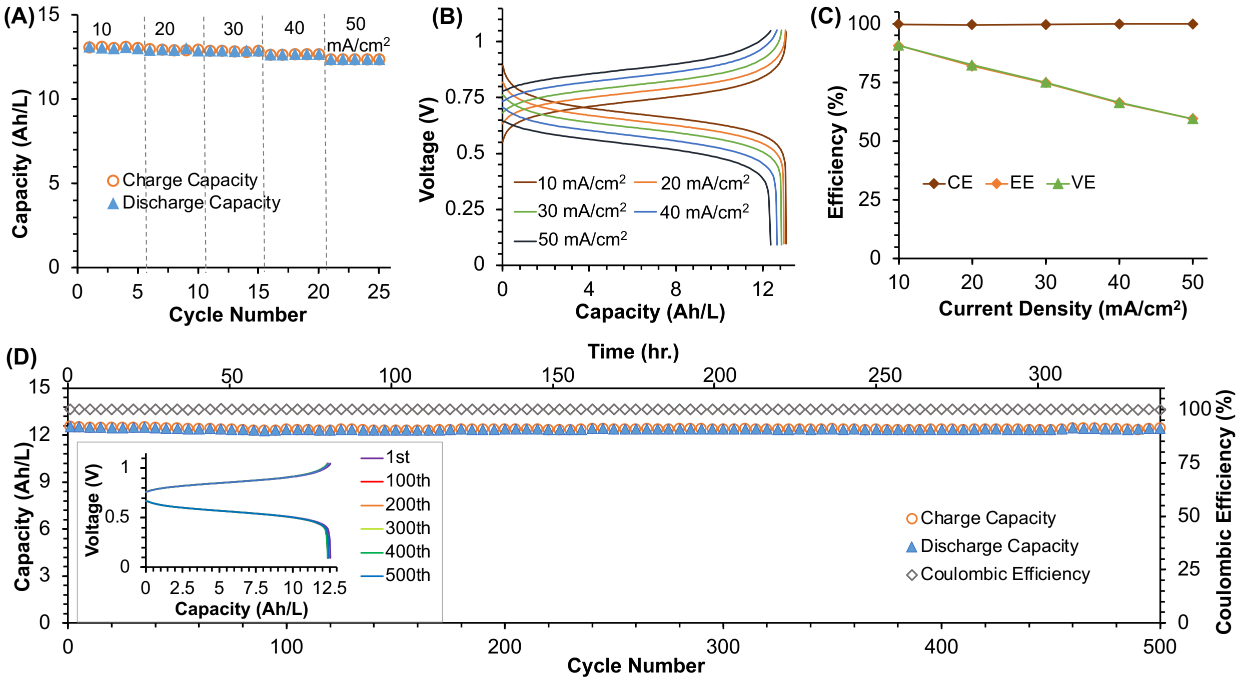

Figure S15. Full-cell RFB studies of the ***C₃*-FcNCl**/(NPr)$_2$VCl$_4$ AORFB. (A) Charge/discharge capacity versus cycling number at 10 – 50 mA·cm^{-2} current densities. (B) Representative charge and discharge profiles of the ***C₃*-FcNCl**/(NPr)$_2$VCl$_4$ AORFB under different current densities. (C) Coulombic efficiency (CE), energy efficiency (EE), and voltage efficiency (VE) of the ***C₃*-FcNCl**/(NPr)$_2$VCl$_4$ AORFB under each current density. (D) Extended 500 cycles testing data of the ***C₃*-FcNCl**/(NPr)$_2$VCl$_4$ AORFB at 40 mA·cm^{-2}, (inset) representative charge and discharge profiles of selected cycles. Condition: catholyte, 0.50 M ***C₃*-FcNCl** in 1.00 M NH_4Cl; anolyte, 0.50 M (NPr)$_2$VCl$_4$ in 1.00 M NH_4Cl; Selemion AMV anion-exchange membrane; pH was adjusted to 7.0 using diluted NH_3•H_2O or HCl; 25 ^{o}C.

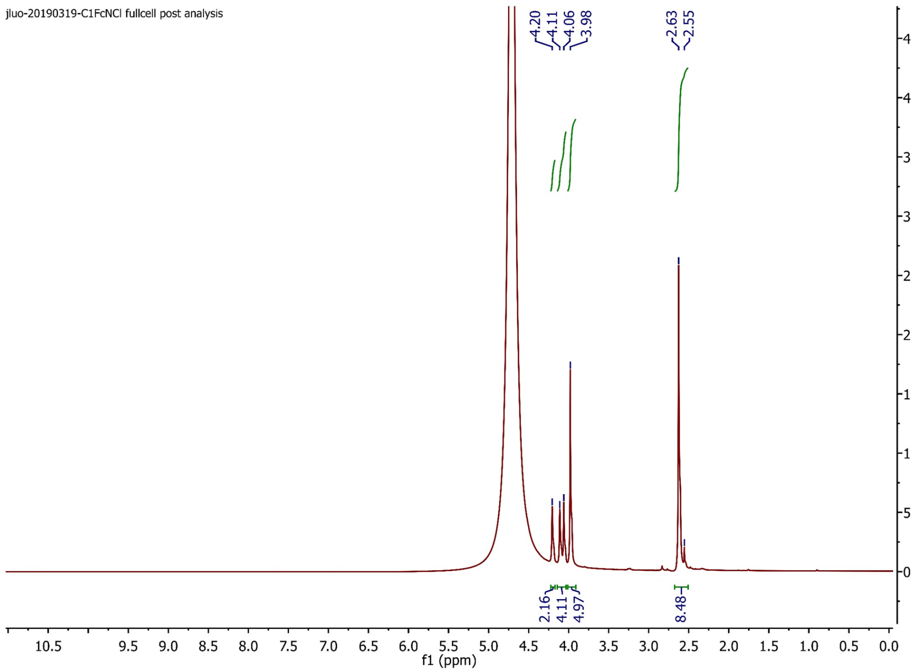

Figure S16. ^{1}H-NMR spectrum of the ***C$_1$*-FcNCl** catholyte after 500 charge/discharge cycles of ***C$_1$*-FcNCl**/(NPr)$_2$VCl$_4$ AORFB.

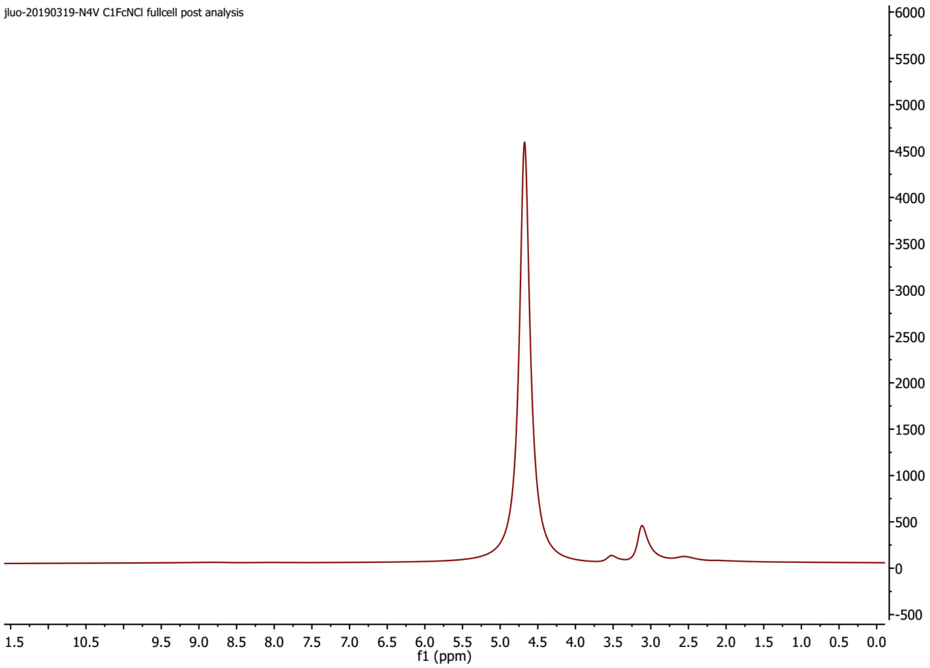

Figure S17. ^{1}H-NMR spectrum of the (NPr)$_2$VCl$_4$ anolyte after 500 charge/discharge cycles of ***C$_1$*-FcNCl**/(NPr)$_2$VCl$_4$ AORFB.

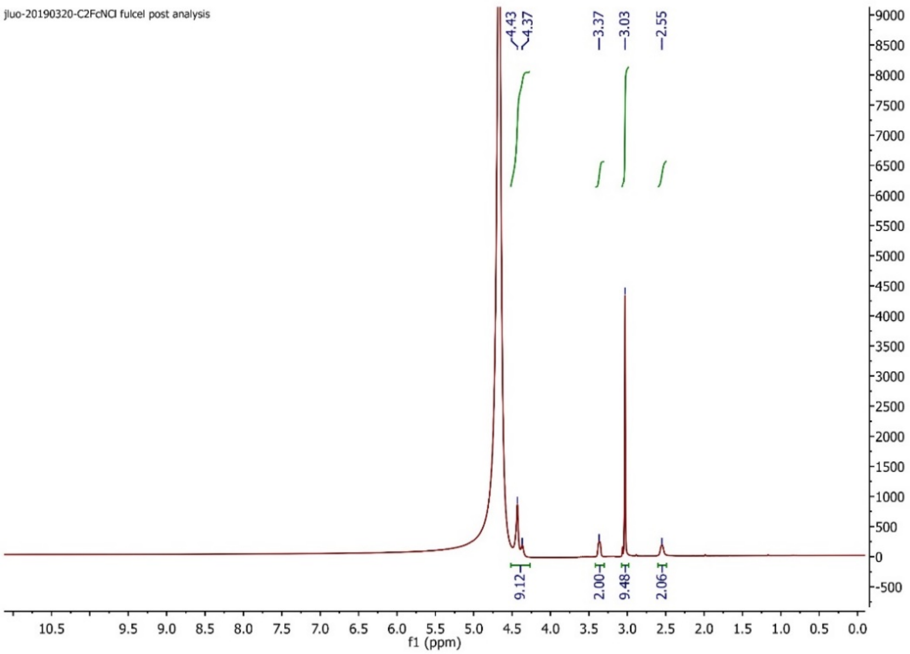

Figure S18. ^{1}H-NMR spectrum of the ***C*₂-FcNCl** catholyte after 500 charge/discharge cycles of ***C*₂-FcNCl**/(NPr)$_2$VCl$_4$ AORFB.

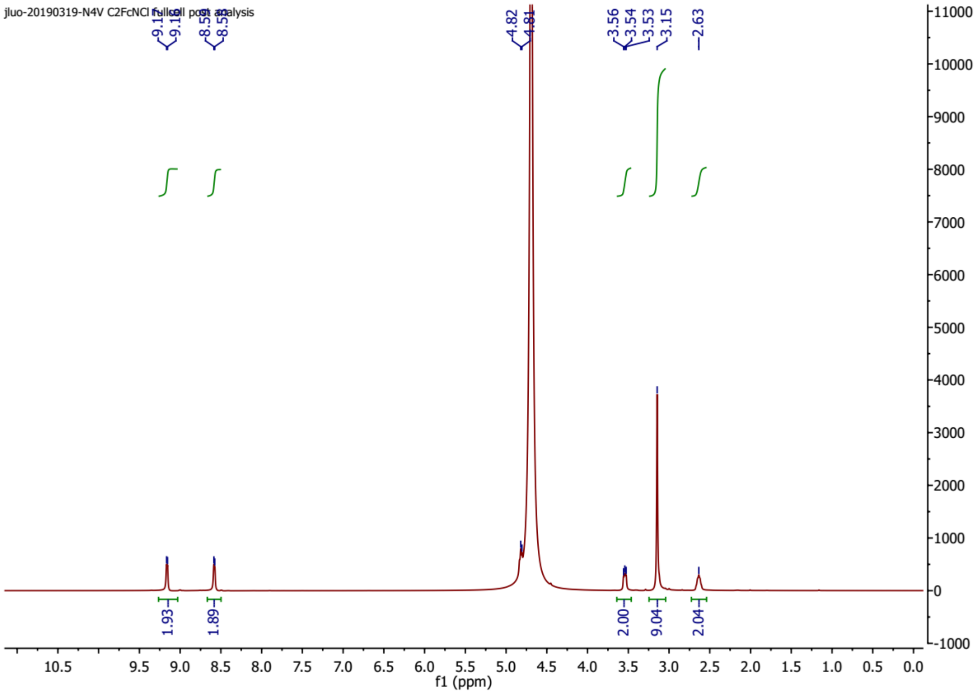

Figure S19. ^{1}H-NMR spectrum of the (NPr)$_2$VCl$_4$ anolyte after 500 charge/discharge cycles of ***C*₂-FcNCl**/(NPr)$_2$VCl$_4$ AORFB.

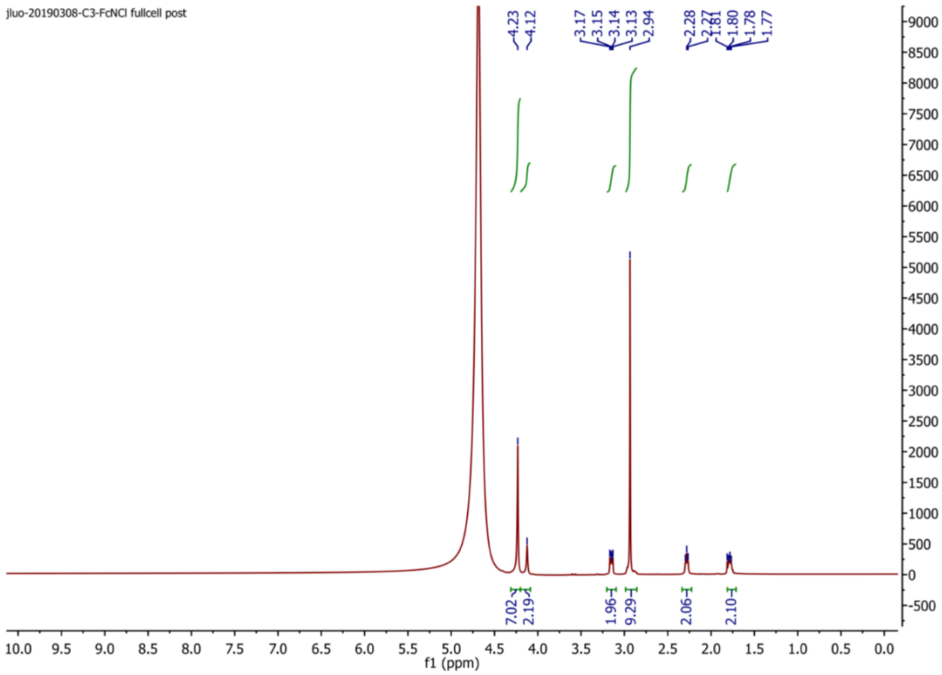

Figure S20. ^{1}H-NMR spectrum of the ***C₃*-FcNCl** catholyte after 500 charge/discharge cycles of ***C₃*-FcNCl**/(NPr)$_2$VCl$_4$ AORFB.

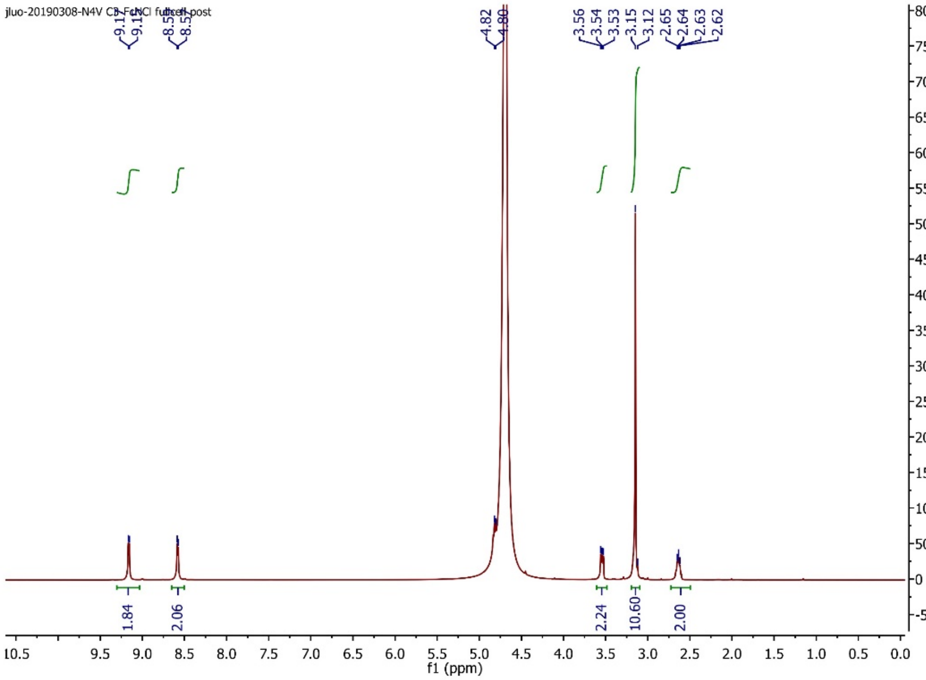

Figure S21. ^{1}H-NMR spectrum of the (NPr)$_2$VCl$_4$ anolyte after 500 charge/discharge cycles of ***C₃*-FcNCl**/(NPr)$_2$VCl$_4$ AORFB.

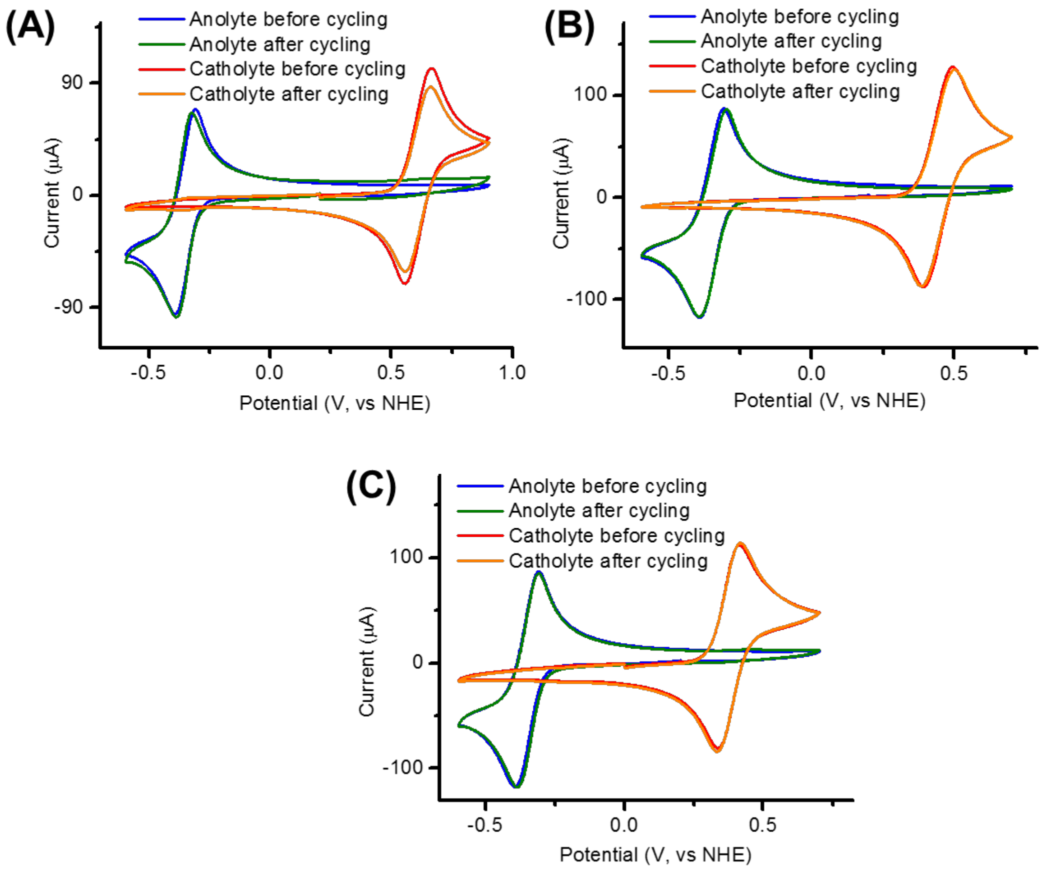

Figure S22. Post-cycling CV analysis of the **C_x-FcNCl**/(NPr)$_2$VCl$_4$ AORFBs. (A) **C_1-FcNCl**/(NPr)$_2$VCl$_4$; (B) **C_2-FcNCl**/(NPr)$_2$VCl; and (C) **C_3-FcNCl**/(NPr)$_2$VCl$_4$ after 500 charge/discharge cycles.

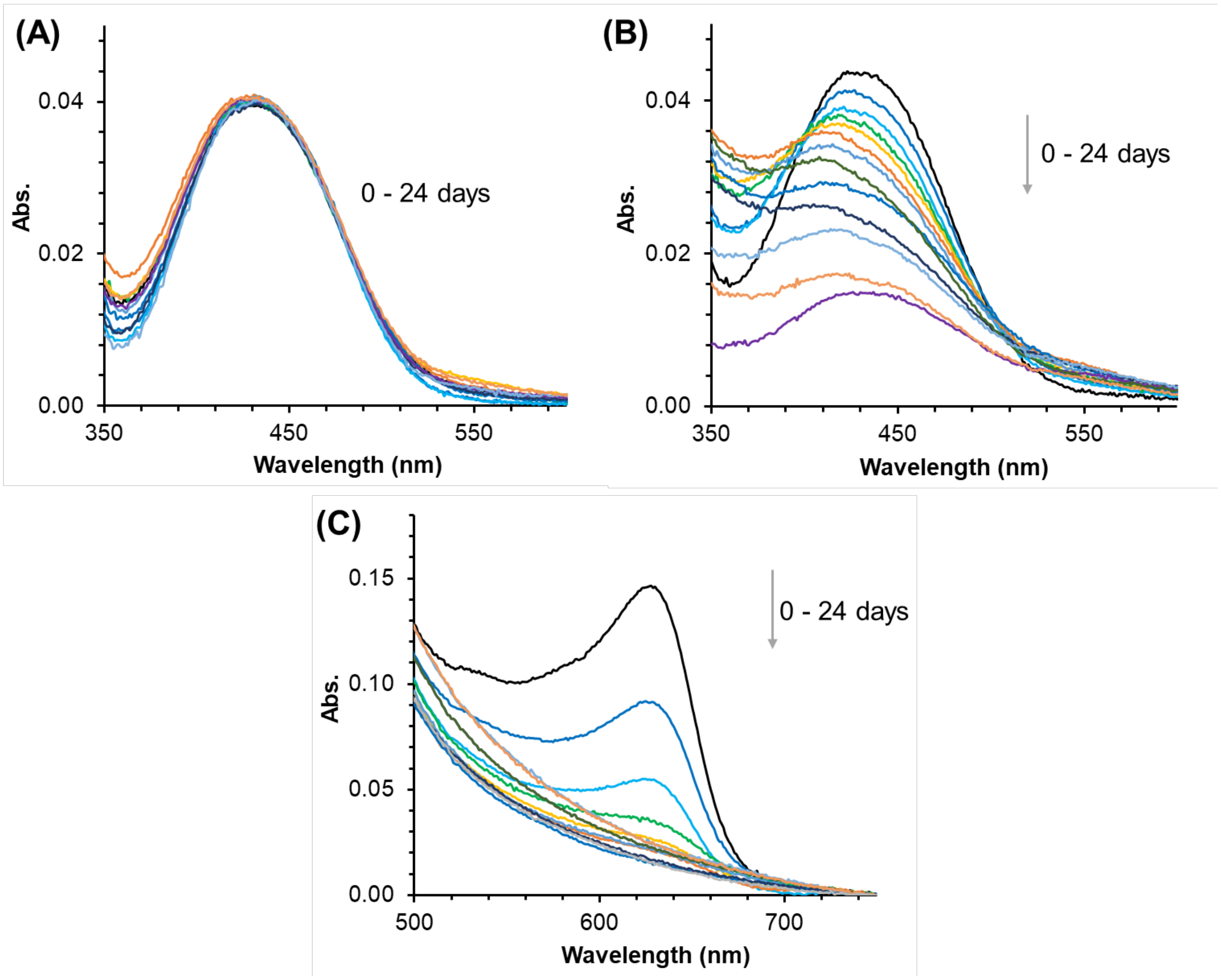

Figure S23. UV-Vis stability studies of 0.4 mM **C_1-FcNCl** catholyte in water for 24 days. (A) Discharged state **[C_1-FcN]$^+$** under dark; (B) Discharged state **[C_1-FcN]$^+$** under ambient light exposure; and (C) Charged state **[C_1-FcN]$^{2+}$** under ambient light exposure.

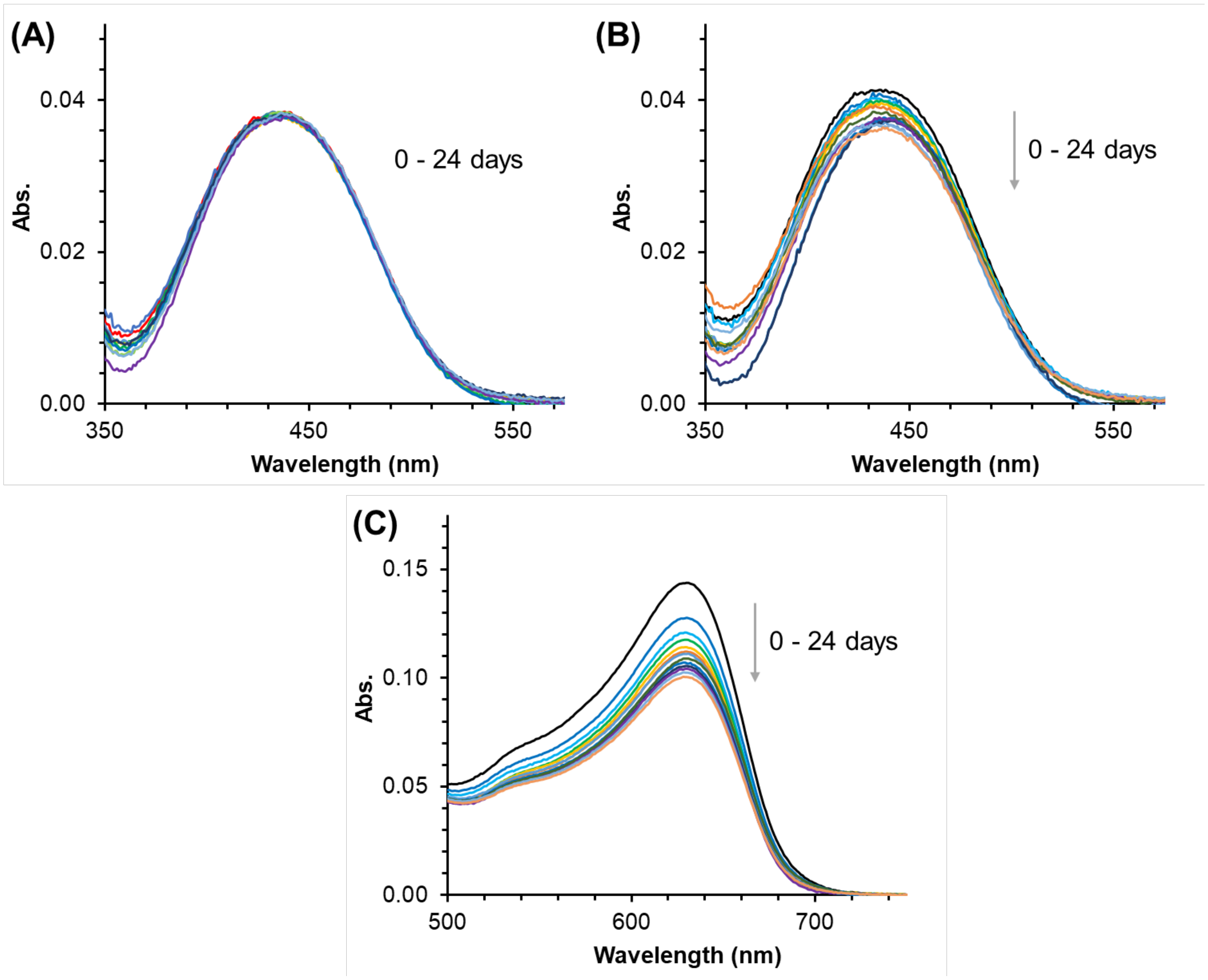

Figure S24. UV-Vis stability studies of 0.4 mM **C_2-FcNCl** catholyte in 24 days. (A) Discharged state **[C_2-FcN]$^{+}$** under dark; (B) Discharged state **[C_2-FcN]$^{+}$** under ambient light exposure; and (C) Charged state **[C_2-FcN]$^{2+}$** under ambient light exposure.

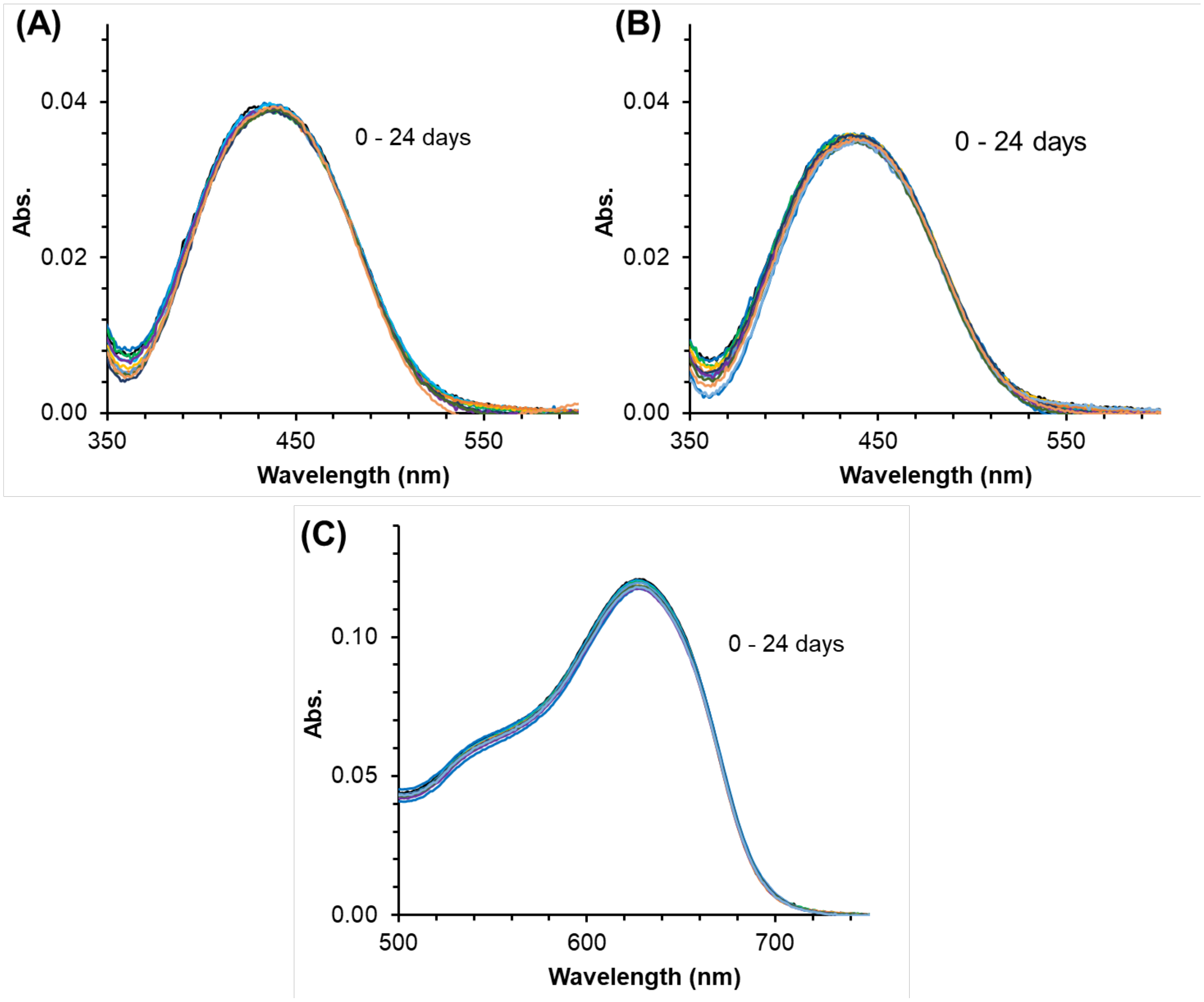

Figure S25. UV-vis stability studies of 0.4 mM **C_3-FcNCl** catholyte in 24 days. (A) Discharged state **[C_3-FcN]**$^+$ under dark; (B) Discharged state **[C_3-FcN]**$^+$ under ambient light exposure; and (C) Charged state **[C_3-FcN]**$^{2+}$ under ambient light exposure.

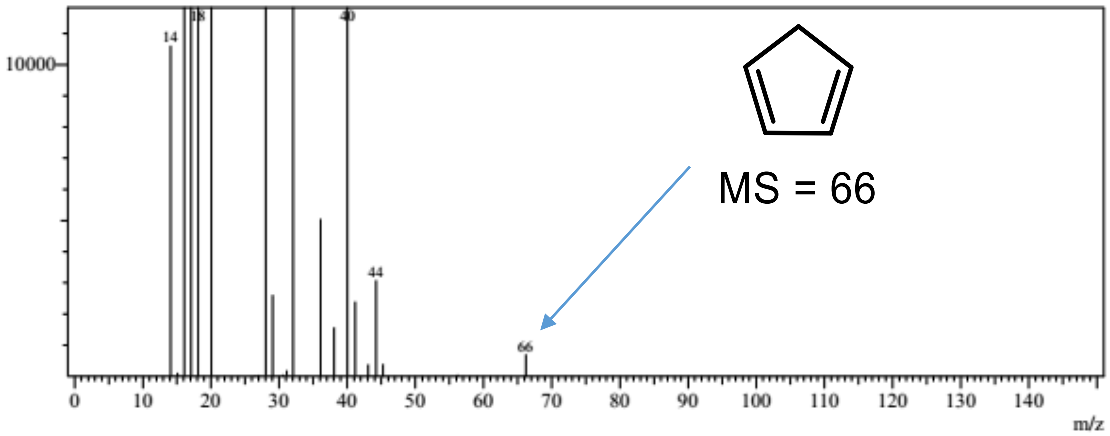

Figure S26. GC-MS spectrum of the gas phase sample in the cycled **C_1-FcNCl** half-cell RFB.

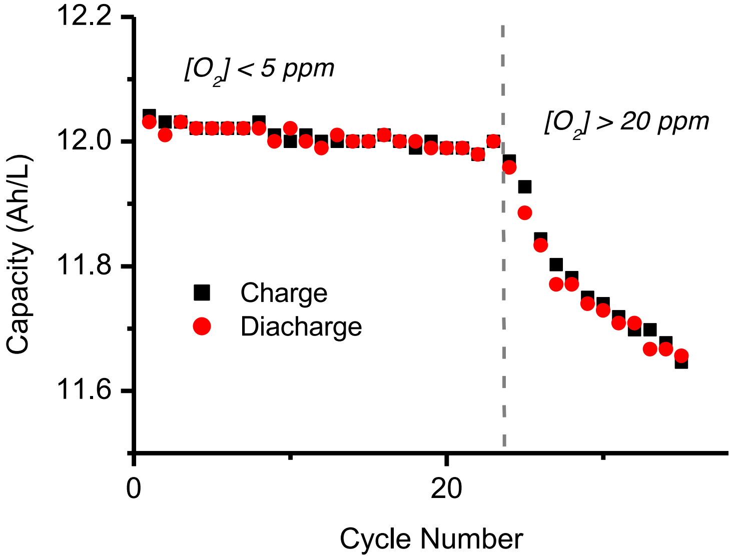

Figure S27. The charge/discharge cycling data of 0.50 M **C_1-FcNCl** half-cell RFB at 40 mA·cm^{-2} current density under different O_2 levels.

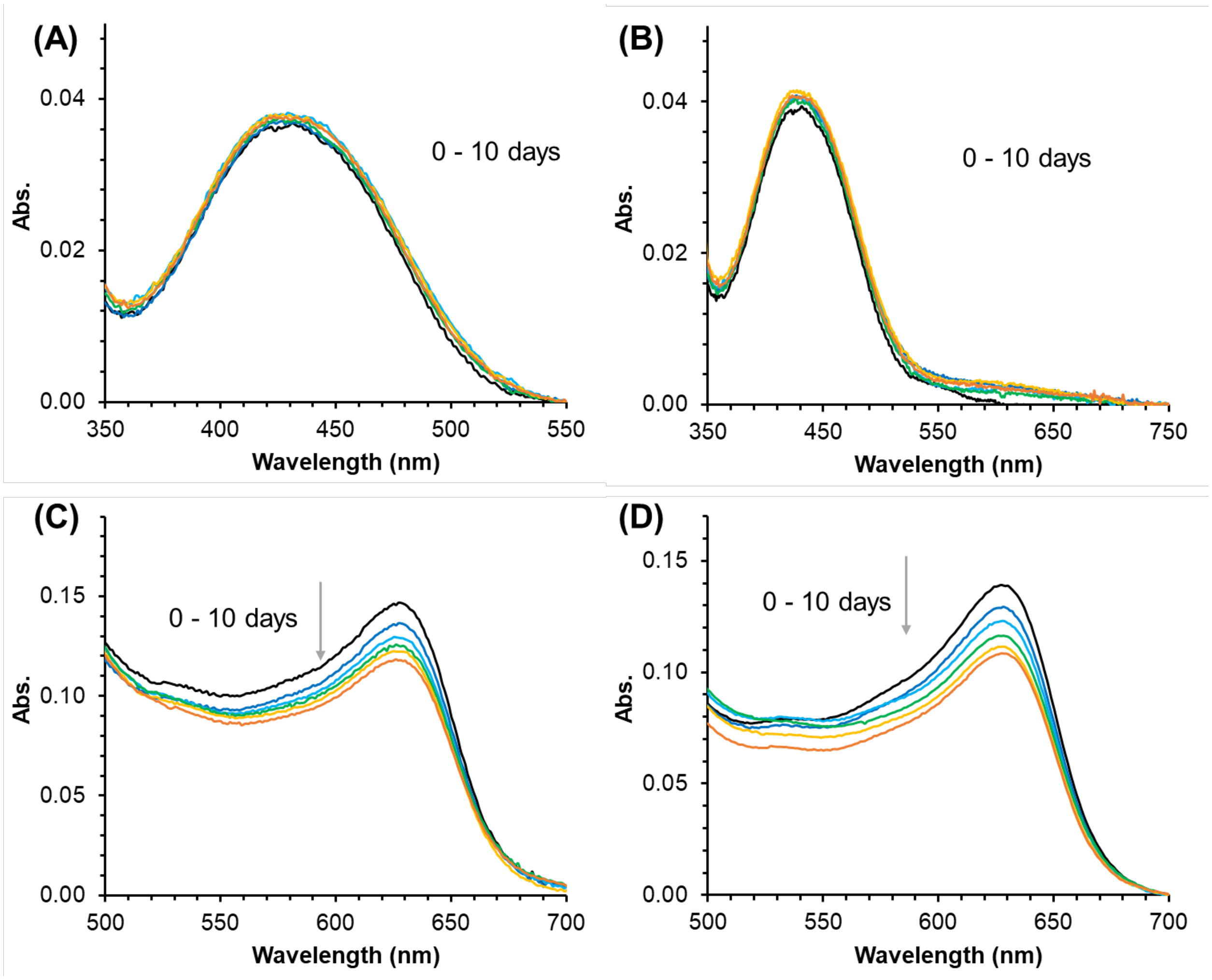

Figure S28. UV-Vis stability studies of 0.4 mM ***C_1*-FcNCl** catholyte under N_2 and O_2 in 10 days. (A) Discharged state **[C_1-FcN]**$^+$ under dark in N_2 atmosphere; (B) Discharged state **[C_1-FcN]**$^+$ under dark in O_2 atmosphere; (C) Charged state **[C_1-FcN]**$^{2+}$ under dark in N_2 atmosphere; (D) Charged state **[C_1-FcN]**$^{2+}$ under dark in O_2 atmosphere.

Notes for Figure S28: In Figure 28B, the absorption at 625 nm showed no change during 10 days, which indicates the discharged state **[C_1-FcN]**$^+$ is not O_2 sensitive. In Figure 28C and 28D, the absorption decayed 18.6% under N_2 atmosphere and 24.3% under O_2, respectively, which indicates that O_2 can slightly accelerate the decomposition of charged state **[C_1-FcN]**$^{2+}$.

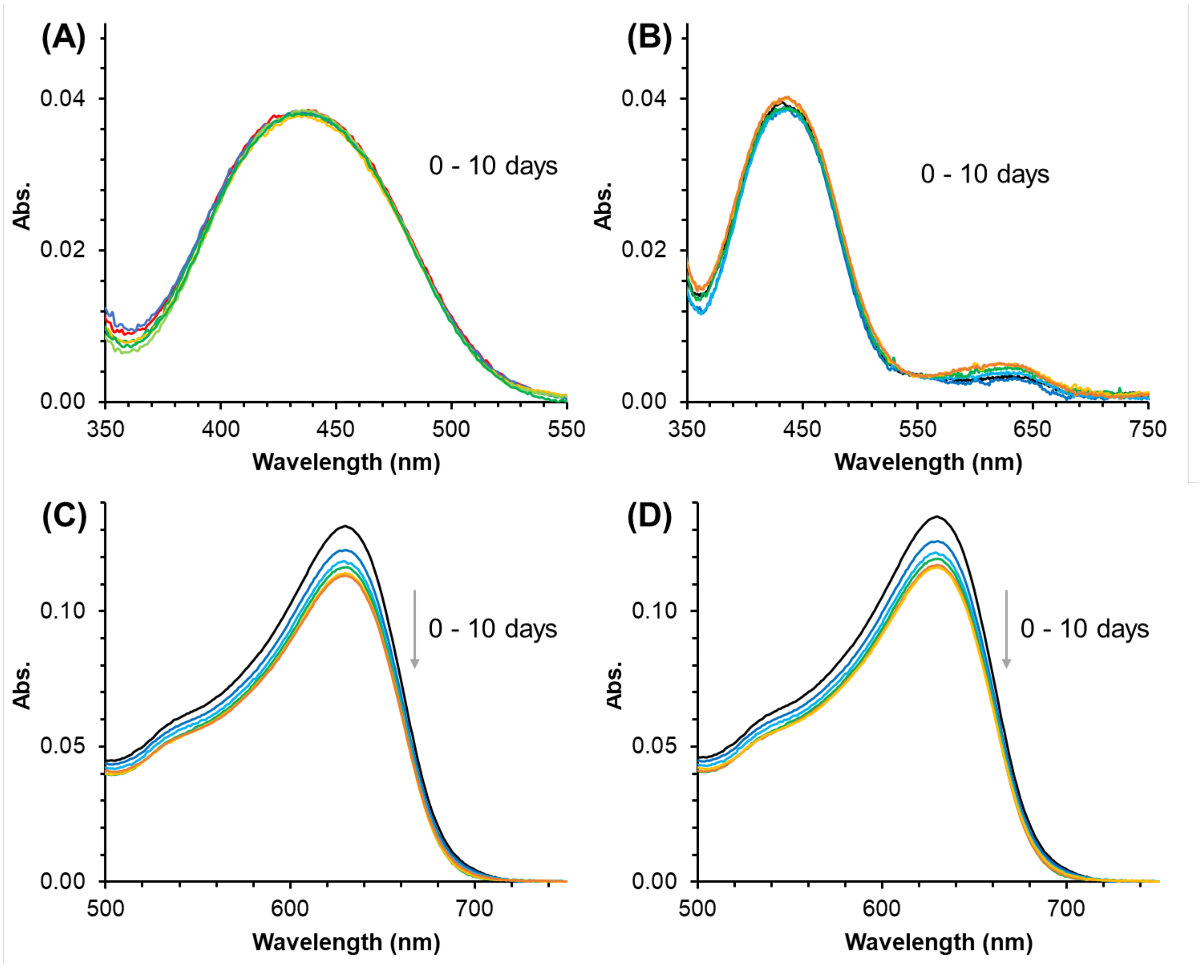

Figure S29. UV-Vis stability studies of 0.4 mM ***C_2*-FcNCl** catholyte under N_2 and O_2 in 10 days. (A) Discharged state **[*C_2*-FcN]$^+$** under dark in N_2 atmosphere; (B) Discharged state **[*C_2*-FcN]$^+$** under dark in O_2 atmosphere; (C) Charged state **[*C_2*-FcN]$^{2+}$** under dark in N_2 atmosphere; (D) Charged state **[*C_2*-FcN]$^{2+}$** under dark in O_2 atmosphere.

Notes for Figure S29: In Figure 29B, an absorption peak at 630 nm showed up in 10 days, which means the discharged state **[*C_2*-FcN]$^+$** is partially oxidized by O_2. In Figure 29C and 29D, the absorption decayed 13.7% under N_2 atmosphere and 13.3% under O_2, respectively, which indicates that charged state **[*C_2*-FcN]$^{2+}$** is not O_2 sensitive.

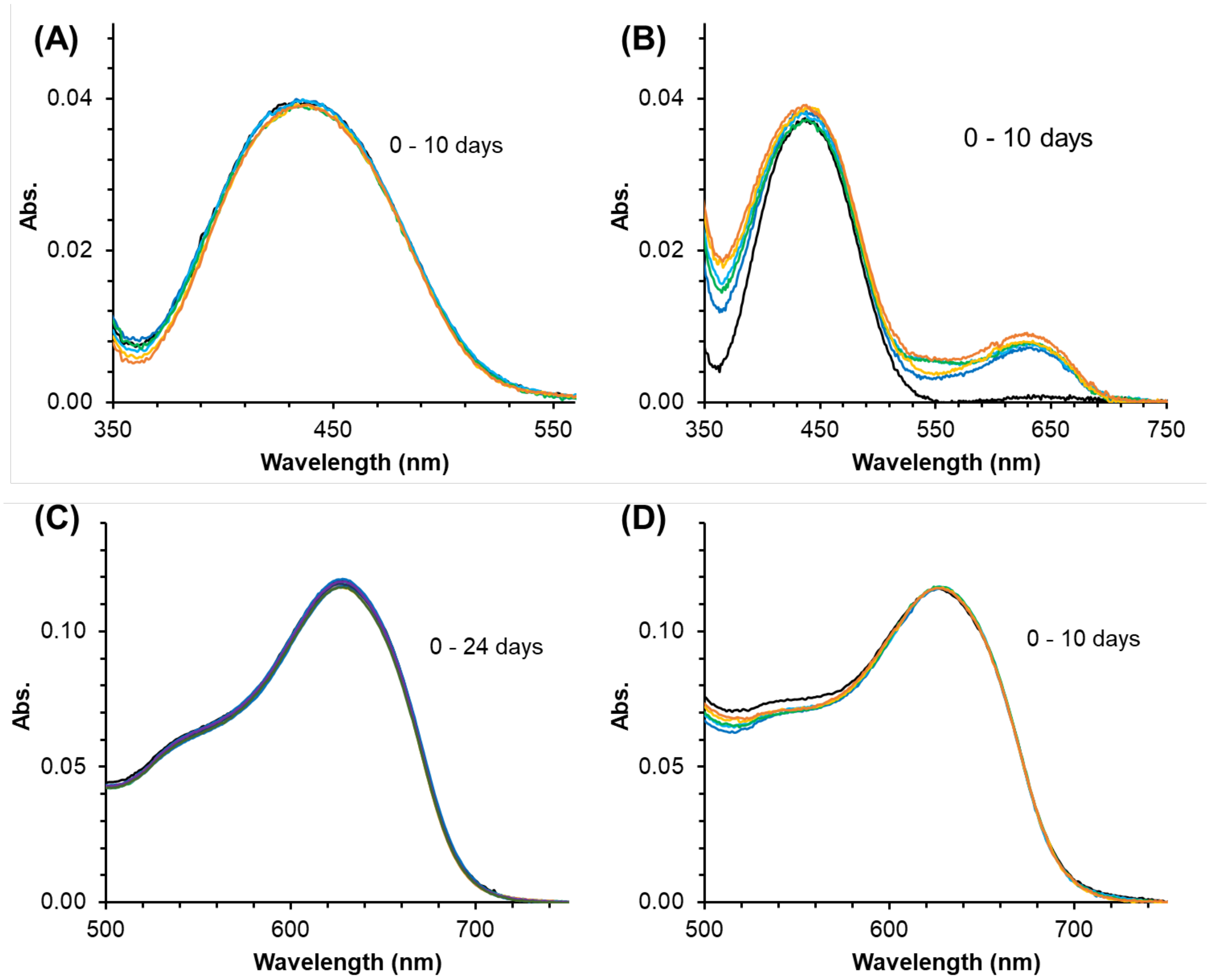

Figure S30. UV-vis stability studies of 0.4 mM ***C_3*-FcNCl** catholyte under N_2 and O_2 in 10 days. (A) Discharged state **[*C_3*-FcN]$^+$** under dark in N_2 atmosphere; (B) Discharged state **[*C_3*-FcN]$^+$** under dark in O_2 atmosphere; (C) Charged state **[*C_3*-FcN]$^{2+}$** under dark in N_2 atmosphere; (D) Charged state **[*C_3*-FcN]$^{2+}$** under dark in O_2 atmosphere.

Notes for Figure S30: In Figure 30B, an absorption peak at 630 nm showed an increase in 10 days, which means the discharged state **[*C_3*-FcN]$^+$** is partially oxidized by O_2.

3. NMR Spectrum

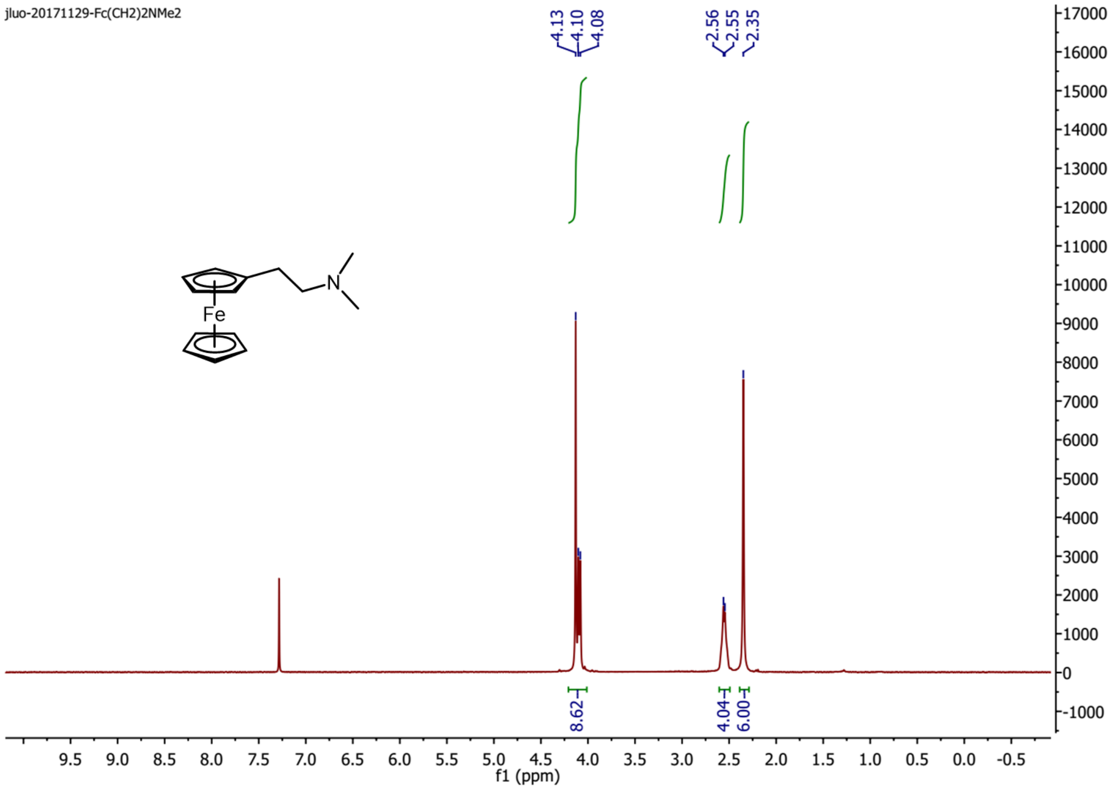

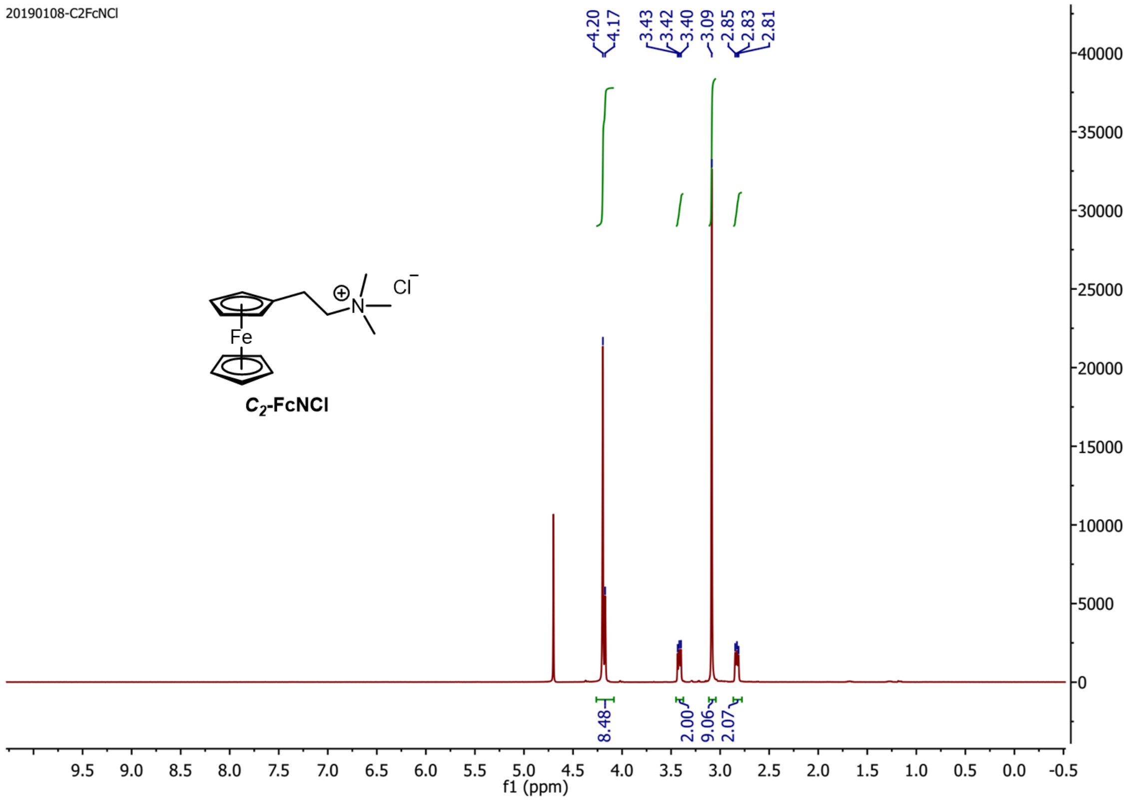

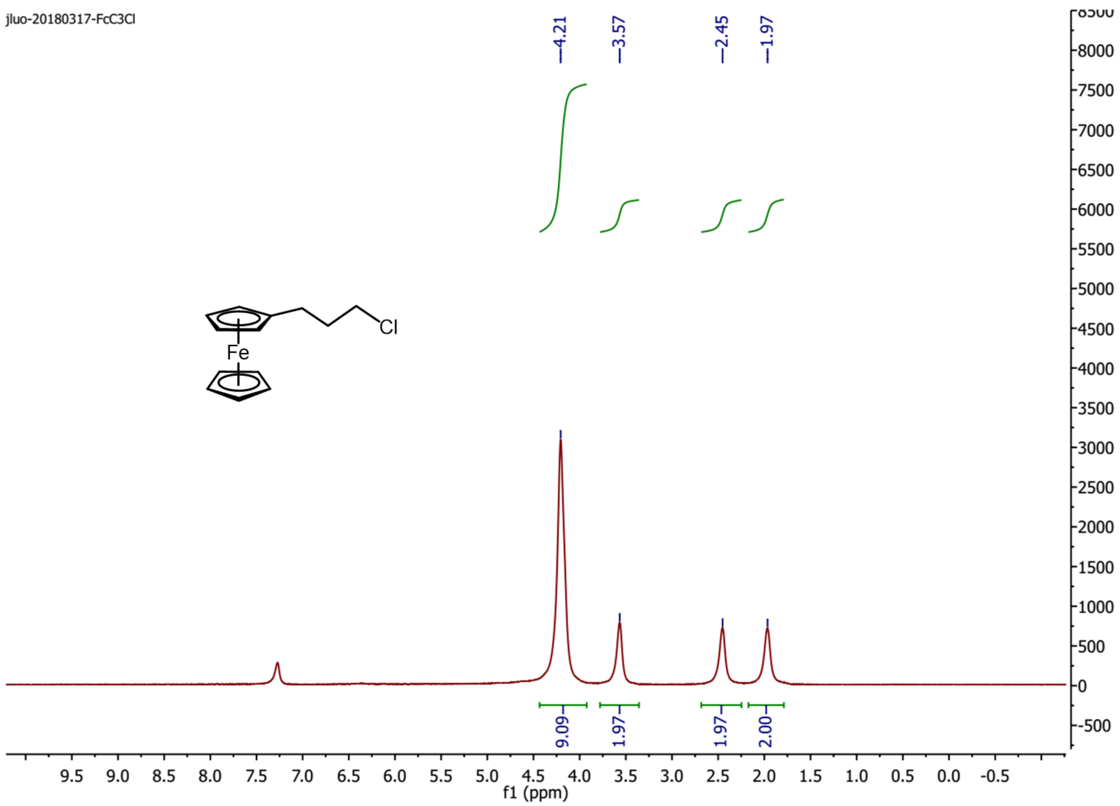
jluo-20180317-FcC3Cl
4.21
3.57
2.45
1.97
Fe
Cl
9.09
1.97
1.97
2.00
9.5 9.0 8.5 8.0 7.5 7.0 6.5 6.0 5.5 5.0 4.5 4.0 3.5 3.0 2.5 2.0 1.5 1.0 0.5 0.0 -0.5
f1 (ppm)
8500 8000 7500 7000 6500 6000 5500 5000 4500 4000 3500 3000 2500 2000 1500 1000 500 0 -500

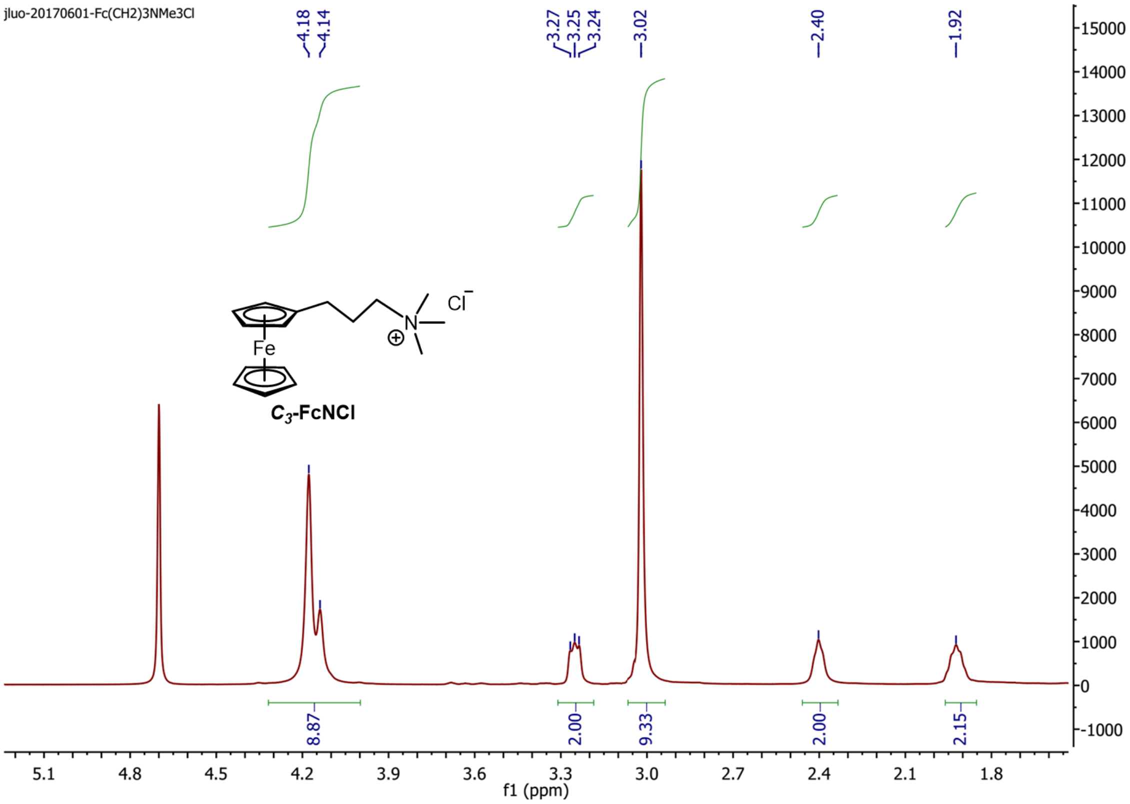
jluo-20170601-Fc(CH2)3NMe3Cl
4.18
4.14
3.27
3.25
3.24
3.02
2.40
1.92
Fe
N
⊕
Cl⁻
C3-FcNCl
8.87
2.00
9.33
2.00
2.15
5.1 4.8 4.5 4.2 3.9 3.6 3.3 3.0 2.7 2.4 2.1 1.8
f1 (ppm)
15000 14000 13000 12000 11000 10000 9000 8000 7000 6000 5000 4000 3000 2000 1000 0 -1000

4. References:

(1) DeBruler, C.; Hu, B.; Moss, J.; Liu, X.; Luo, J.; Sun, Y.; Liu, T. L. Designer Two-Electron Storage Viologen Anolyte Materials for Neutral Aqueous Organic Redox Flow Batteries. *Chem* **2017**, *3*, 961-978.

(2) Hu, B.; Tang, Y.; Luo, J.; Grove, G.; Guo, Y.; Liu, T. L. Improved radical stability of viologen anolytes in aqueous organic redox flow batteries. *Chemical Communications* **2018**, *54*, 6871-6874.

(3) Beh, E. S.; De Porcellinis, D.; Gracia, R. L.; Xia, K. T.; Gordon, R. G.; Aziz, M. J. A Neutral pH Aqueous Organic–Organometallic Redox Flow Battery with Extremely High Capacity Retention. *ACS Energy Letters* **2017**, *2*, 639-644.